Journal of Computational Physics 229 (2010) 2139–2158

Contents lists available at ScienceDirect

Journal of Computational Physics

journal homepage: www.elsevier.com/locate/jcp

Entropy considerations in numerical simulations of non-equilibrium rarefied flows

S. Chigullapalli [a], A. Venkattraman [a], M.S. Ivanov [b], A.A. Alexeenko [a,*]

[a] School of Aeronautics and Astronautics, Purdue University, West Lafayette, IN 47907, United States
[b] Khristianovich Institute of Theoretical and Applied Mechanics, Novosibirsk 630090, Russia

ARTICLE INFO

Article history:
Received 6 July 2009
Received in revised form 13 November 2009
Accepted 17 November 2009
Available online 26 November 2009

Keywords:
Rarefied gas flows
Kinetic theory
Non-continuum effects
Numerical methods
Shock waves

ABSTRACT

Non-equilibrium rarefied flows are encountered frequently in supersonic flight at high altitudes, vacuum technology and in microscale devices. Prediction of the onset of non-equilibrium is important for accurate numerical simulation of such flows. We formulate and apply the discrete version of Boltzmann's *H*-theorem for analysis of non-equilibrium onset and accuracy of numerical modeling of rarefied gas flows. The numerical modeling approach is based on the deterministic solution of kinetic model equations. The numerical solution approach comprises the discrete velocity method in the velocity space and the finite volume method in the physical space with different numerical flux schemes: the first-order, the second-order minmod flux limiter and a third-order WENO schemes. The use of entropy considerations in rarefied flow simulations is illustrated for the normal shock, the Riemann and the two-dimensional shock tube problems. The entropy generation rate based on kinetic theory is shown to be a powerful indicator of the onset of non-equilibrium, accuracy of numerical solution as well as the compatibility of boundary conditions for both steady and unsteady problems.

1. Introduction

In regions of non-equilibrium, which are encountered frequently in supersonic flows at high altitudes and flows expanding into vacuum, the macroscopic constitutive laws based on the continuum hypothesis tend to breakdown. The limits on the conventional mathematical models are usually understood based on the Knudsen number ($Kn = \lambda/L$) where λ is the average distance traveled by the molecules between collisions, or the mean free path, and L is the characteristic length scale. When the flow gradients are large, the length scale is of the same order as the mean free path and the transport terms in the continuum equations breakdown. When the continuum approximations are invalid, as in the case of a flow within a normal shock wave and many other flow conditions, a model at the molecular level is required.

Mathematically, the motion of molecules in dilute gas is described by the Boltzmann equation which is valid for the entire spectrum of Knudsen numbers. However, due to the multidimensionality of the phase space, which includes both physical coordinates and velocity coordinates, and the complex non-linearity of the collision term, the numerical solution of the full Boltzmann equation is challenging for practical problems. One approach to alleviate these difficulties has been to apply hybrid continuum and rarefied flow modeling. For example, a coupled solution of Euler equations in the inviscid flow domain with the direct simulation Monte Carlo (DSMC) solution in non-equilibrium regions has been developed in Ref. [1]. Another

* Corresponding author. Tel.: +1 765 496 1864; fax: +1 765 494 0307.
E-mail address: alexeenk@purdue.edu (A.A. Alexeenko).

0021-9991/$ - see front matter © 2009 Elsevier Inc. All rights reserved.
doi:10.1016/j.jcp.2009.11.027

approach for hybrid continuum/rarefied flow simulations has been presented in Ref. [2], where both domains are solved with particle-based methods. Alternatively, two deterministic numerical methods were used for both continuum and rarefied regions in Ref. [3].

In all of the above hybrid continuum/rarefied simulations, a parameter characterizing the onset of non-equilibrium is needed. A number of continuum breakdown parameters have been proposed in the past to predict the onset of non-equilibrium such as the local Knudsen number which is obtained as the ratio of a macroscopic flow parameter, like density or temperature, to its gradient. Though these parameters provide an indication of the onset of rarefied flow effects, there is no direct relation between such parameters and the physics of non-equilibrium. In this regard, the main goal of this paper is to investigate the use of entropy generation rate as an indicator of the onset of non-equilibrium. Additionally, we show that entropy considerations in the deterministic simulations of rarefied flows are useful for analysis of accuracy of numerical solutions. In particular, entropy-based analysis of numerical errors is developed with the use of a discrete version of Boltzmann's *H*-theorem.

It has been proposed in Ref. [4] that the entropy generation rate is likely to be one of the fundamental and most important parameters to predict the onset of non-equilibrium. Thermodynamic equilibrium is characterized by zero entropy generation, and non-equilibrium can be identified by positive entropy generation. That is, a system progresses from one state of thermodynamic equilibrium to a new state of thermodynamic equilibrium through the generation of entropy. Therefore, a single parameter, entropy generation, is identified with thermodynamic non-equilibrium and therefore includes all of the physics which will cause the continuum equations to break down. Also, due to its relation to the second law of thermodynamics, entropy generation can capture non-physical numerical solutions that result from discretization errors.

The remainder of the paper is organized as follows: In Section 2, we present details of calculation of entropy, entropy generation rate and its relation to the onset of non-equilibrium. In Section 3, we discuss briefly, the Boltzmann model kinetic equation and the collision models considered in this work, and in Section 4, we describe the numerical methods including high-order flux schemes and time integration schemes. Section 5 presents and discusses the results of entropy-based analysis of numerical simulations for the normal shock wave, and one-dimensional and two-dimensional shock tube problems.

2. Entropy generation rate

The second law of thermodynamics postulates the existence of a state function called entropy and describes its properties. However, the most fundamental expression for entropy is given by the Boltzmann relation derived from statistical mechanics

$$S = k \ln \Omega \tag{1}$$

where S is the entropy, k is the Boltzmann constant and Ω is the statistical multiplicity of the gas. The quantity Ω represents the total number of possible ways in which the total energy of the system can be distributed. In this paper, only the translational component of entropy is discussed since all computations reported are for a monatomic gas, argon.

The expression for translational entropy in terms of the velocity distribution function f can be derived (Eq. (37) in Ref. [5]) as

$$S_{tr} = k \int_{-\infty}^{\infty} f(\vec{c}) \left[1 - \ln \left(\frac{h^3 f(\vec{c})}{m^3} \right) \right] d\vec{c} \tag{2}$$

where h is the Planck constant, m is the atomic mass of the gas and c is the molecular velocity.

The entropy generation rate based on a kinetic description in terms of the velocity distribution function can be obtained using the moment transfer equation [18]. The final expression [5] for the entropy generation rate based on kinetic theory is given by

$$\dot{S} = \frac{\partial S}{\partial t} + \nabla \cdot \left(k \int_{-\infty}^{\infty} \vec{c} f(\vec{c}) \left[1 - \ln \left(\frac{h^3 f(\vec{c})}{m^3} \right) \right] d\vec{c} \right) \tag{3}$$

Since the formulation of this parameter involves the utilization of only statistical mechanics and kinetic theory, there are no inherent mathematical limitations in its calculation. In this paper, Eq. (3) will be referred to as the *Kinetic Theory-lhs* expression for entropy generation rate.

For small deviations from local equilibrium, the entropy generation rate can also be calculated as a function of macroparameters only. This will be referred to as the *Gas Dynamic* expression [6,7] for entropy generation rate and is given by

$$\dot{S} = \frac{\Phi}{T} + \frac{\kappa}{T^2} (\nabla T \cdot \nabla T) \tag{4}$$

where Φ is the viscous dissipation function and $\kappa = \mu C_p / Pr$. For one-dimensional compressible flows, it can be simplified as

$$\dot{S} = \frac{4}{3} \frac{\mu}{T} \left(\frac{\partial u}{\partial x} \right)^2 + \frac{\kappa}{T^2} \left(\frac{\partial T}{\partial x} \right)^2 \tag{5}$$

Schrock et al. [5] have shown that the location of initial increase in entropy production for a stationary normal shock wave predicted by the Navier–Stokes equations is few mean free paths downstream of the location predicted by the DSMC technique, thereby indicating that the breakdown parameters based on continuum data may fail to capture the non-equilibrium effects completely.

3. Boltzmann's model kinetic equations

One class of model equations which are widely used to solve non-equilibrium rarefied flows are the Bhatnagar–Gross–Krook (BGK) type equations [8,9] with a relaxation-type collision term. These equations are easier to solve when compared to the original Boltzmann equation though the number of dimensions in the phase space remains the same as in the Boltzmann equation. They also satisfy the H-theorem (which states that the production of entropy is always non-negative) and reproduces a Maxwellian phase density at equilibrium [10]. According to the model kinetic equations, the phase density $f(x,\vec{c},t)$ is governed by the equation,

$$\frac{\partial f}{\partial t}+\vec{c}\cdot\frac{\partial f}{\partial \vec{x}}=-\nu(f-f_0) \tag{6}$$

One of the collision relaxation models that is widely used is the ellipsoidal-statistical model (ES-BGK) [11] where $f_0=f_G$ is an anisotropic Gaussian given by

$$f_G=\frac{\rho}{\sqrt{det(2\pi\mathbb{T})}}e^{\left[-\frac{1}{2}(\vec{c}-\vec{u})^T\mathbb{T}^{-1}(\vec{c}-\vec{u})\right]} \tag{7}$$

where

$$\begin{aligned}
&\vec{c}-\vec{u}=[c_x-u,c_y-v,c_z-w]\\
&\rho\mathbb{T}=\frac{1}{Pr}\rho RTI+\left(1-\frac{1}{Pr}\right)\rho\ominus\\
&\rho\ominus=\langle(\vec{c}-\vec{u})\otimes(\vec{c}-\vec{u})f\rangle\\
&\rho RTI=\langle(\vec{c}-\vec{u})\otimes(\vec{c}-\vec{u})f_\gamma\rangle
\end{aligned}$$

with f_γ being a Gaussian of the form $a\exp(-\Gamma C^2+\gamma_i C_i)$ and ν being the collision frequency given by

$$\nu=\frac{Pr\cdot p}{\mu}$$

It should be observed that the collision frequency, ν, involves the Prandtl number, Pr, as a free parameter. This allows the ES collision model to reproduce transport coefficients, viscosity and thermal conductivity, corresponding to an arbitrary Prandtl number.

The collision term of the BGK model can be obtained as a special case of the ES collision model by substituting $Pr=1$. We indicate this collision term by $-\nu(f-f_\gamma)$.

The expression for the entropy generation rate based on kinetic theory was derived from the Boltzmann equation using the fact that the entropy generation rate is the variation of entropy due to collisions. In DSMC simulations, the variation due to collisions cannot be computed directly, whereas in an approach based on model kinetic equations, the explicit form of the collision term facilitates this rate to be computed directly. The entropy generation rate calculated using the collision term is given by

$$\dot{S}_{coll}=-\nu\int_{-\infty}^{\infty}(f(\vec{c})-f_0(\vec{c}))\ln\left(\frac{h^3f(\vec{c})}{m^3}\right)d\vec{c} \tag{8}$$

with f_0 being an anisotropic Gaussian or an isotropic Gaussian (Maxwellian), depending on the collision model. This term will be referred to as *Kinetic Theory-rhs* expression for entropy generation rate. It should be mentioned that this term will always be positive if the collision model under consideration satisfies the H-theorem.

4. Numerical method

There have been various attempts in the past to apply different numerical schemes to obtain solutions to the model kinetic equations [12]. In general, the numerical method that is applied, should conserve mass, momentum and energy. It should also satisfy Boltzmann's H-theorem and ensure positivity of the solution. Here, we present the numerical method in one spatial dimension and three dimensions in microscopic velocity. The governing kinetic equation (Eq. (6)), when simplified to one-dimension, is given by

$$\frac{\partial f}{\partial t}+c_x\frac{\partial f}{\partial x}=-\nu(f-f_0) \tag{9}$$

The space variable is discretized on a Cartesian grid defined by nodes x_i. The microscopic velocities in the $x,\ y,\ z$ directions, $c_x,\ c_y,\ c_z$, are discretized using a conventional discrete ordinate method with uniform velocity abscissas. In the current formulation, a discrete velocity $(c_x(j_1), c_y(j_2), c_z(j_3))$ of the grid is denoted by c_j , where $j = (j_1, j_2, j_3)$. Finally, we also choose a time discretization with $t = n\Delta t$.

Upon approximation of the model kinetic equation by a Finite Volume Scheme, we obtain

$$\frac{\partial f}{\partial t} = -\frac{1}{\Delta x}\left[F_{i+\frac{1}{2}j} - F_{i-\frac{1}{2}j}\right] - v_i(f_{ij} - f_{0_{ij}}) \tag{10}$$

where $F_{i+1/2}$ and $F_{i-1/2}$ refer to the flux at the left and right faces of the ith cell.

4.1. First-order and second-order flux schemes

The first- and second-order schemes are as described by Mieussens and Struchtrup [12] and are given by

$$F_{i+\frac{1}{2}j} = \frac{1}{2}\left[c_x(f_{i+1j} + f_{ij}) - |c_x|\left(\Delta f_{i+\frac{1}{2}j} - \phi_{i+\frac{1}{2}}, j\right)\right] \tag{11}$$

where $\Delta f_{i+\frac{1}{2}j} = f_{i+1j} - f_{ij}$ and

$$\phi_{i+1/2j} = \begin{cases} 0 & \text{first-order} \\ minmod\left(\Delta f^n_{i-\frac{1}{2}j}, \Delta f^n_{i+\frac{1}{2}j}, \Delta f^n_{i+\frac{3}{2}j}\right) & \text{second-order} \end{cases}$$

The minmod flux limiter used by the second-order scheme is defined [13] as

$$minmod(a,b,c) = \begin{cases} min(a,b,c) & a > 0,\ b > 0,\ c > 0 \\ max(a,b,c) & a < 0,\ b < 0,\ c < 0 \\ 0 & \text{otherwise} \end{cases}$$

4.2. Third-order WENO scheme

The third-order fluxes are computed using the Weighted Essentially Non-Oscillatory (WENO) schemes described by Zhou et al. [14]. Here, we briefly describe only the most important aspects of the scheme. The general form of the numerical fluxes evaluated at the interface using the third-order WENO scheme is given by

$$F_{i+\frac{1}{2}j} = \sum_{\alpha} \omega_\alpha h_f\left(f^-_{i+\frac{1}{2}j}, f^+_{i+\frac{1}{2}j}\right) \tag{12}$$

where ω_α are the weights. h_f, in our computations is the local Lax–Friedrich's flux function, given by

$$h_f\left(f^-_{i+\frac{1}{2}j}, f^+_{i+\frac{1}{2}j}\right) = \frac{1}{2}\left[c_x\left(f^-_{i+\frac{1}{2}j} + f^+_{i+\frac{1}{2}j}\right) - |c_x|\left(f^-_{i+\frac{1}{2}j} - f^+_{i+\frac{1}{2}j}\right)\right] \tag{13}$$

The most important step in incorporating the third-order WENO scheme is the reconstruction step to obtain third-order accurate values of f at the cell interface. Since this section deals with obtaining third-order accurate fluxes in the physical space, we drop the velocity space index j for convenience. For a given cell I_i, we choose stencils $S(i)$ based on cells adjacent to I_i. In each of these stencils, we find a polynomial $p^{(r)}(x)$, where $r = 1, 2$ refers to the stencil index, such that

$$p^{(r)}\left(x_{i+\frac{1}{2}}\right) = f\left(x_{i+\frac{1}{2}}\right) + O(\Delta^2) \tag{14}$$

To find $p^{(r)}\left(x_{i+\frac{1}{2}}\right)$, we compute constants, $c_i^{(r)}$, that depend only on the mesh, such that

$$\begin{aligned} p^{(1)}\left(x_{i+\frac{1}{2}}\right) &= c_1^{(1)} f_{i-1} + c_2^{(1)} f_i \\ p^{(2)}\left(x_{i+\frac{1}{2}}\right) &= c_1^{(2)} f_i + c_2^{(2)} f_{i+1} \end{aligned} \tag{15}$$

The constants $c_i^{(r)}$ can be calculated by using Lagrange polynomials as explained by Shu [15]. Now, we find constants d_r such that a convex combination of $p^{(r)}\left(x_{i+\frac{1}{2}}\right) \Big| r = 1, 2, 3, 4$ is third-order accurate:

$$\sum_{r=1}^{4} d_r p^{(r)}\left(x_{i+\frac{1}{2}}\right) = f\left(x_{i+\frac{1}{2}}\right) + O(\Delta^3) \tag{16}$$

d_r is referred to as the optimum weight of the WENO scheme. However, if the solution $f(x)$ has a discontinuity in some of the stencils, the corresponding weights should be 0. To achieve this, the following form of non-linear weights is introduced

Table 1
Conditions across a normal shock of Mach number $M = 1.4$.

Property	Upstream	Downstream
Density	1.0	1.581
Velocity	1.278	0.808
Temperature	1.0	1.392
Pressure	1.0	2.2

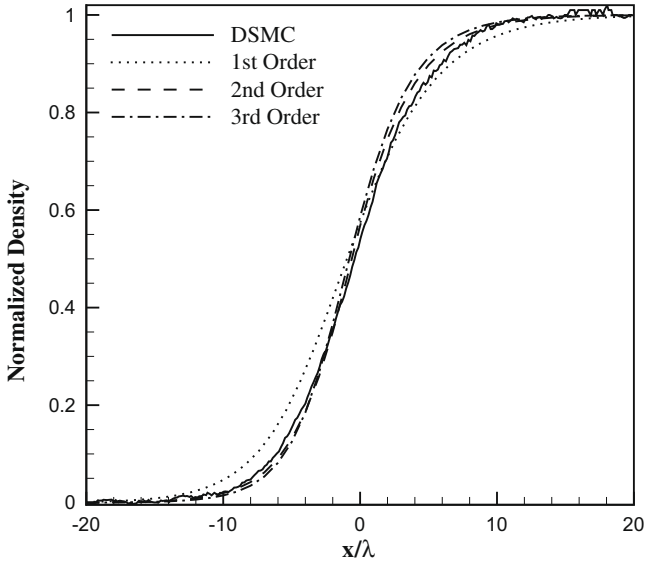

(a) Density profile.

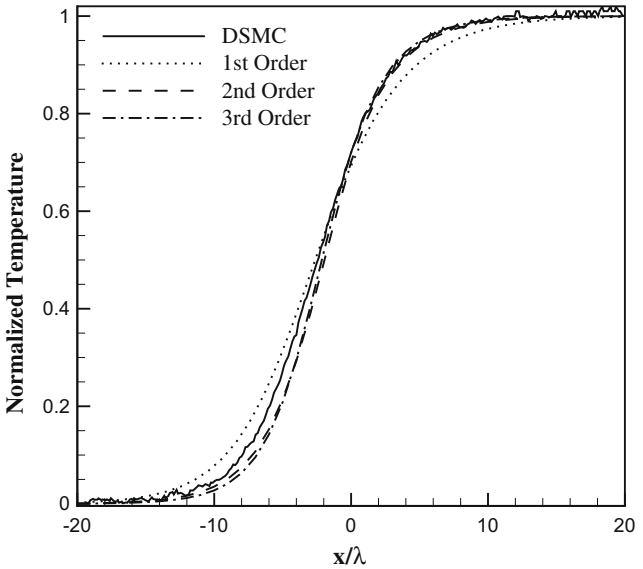

(b) Temperature profile.

Fig. 1. Normal shock structure, $M = 1.4$.

$$\omega_r = \frac{\alpha_r}{\sum_{s=1}^{4} \alpha_s} \tag{17}$$

where

$$\alpha_r = \frac{d_r}{(\epsilon + SI_r)^2} \tag{18}$$

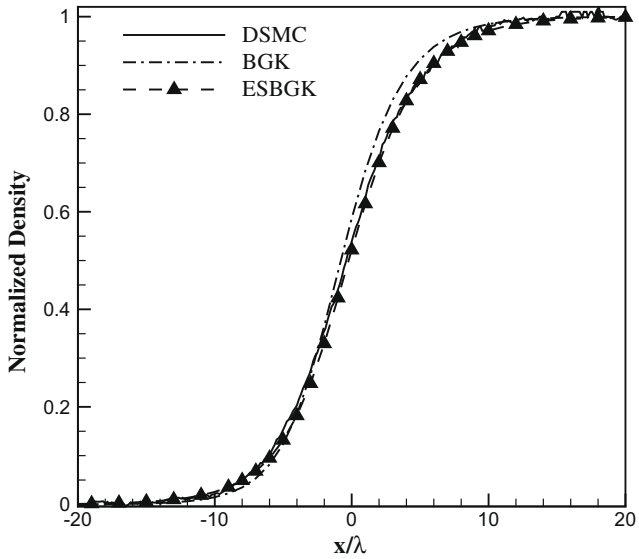

(a) Density profile.

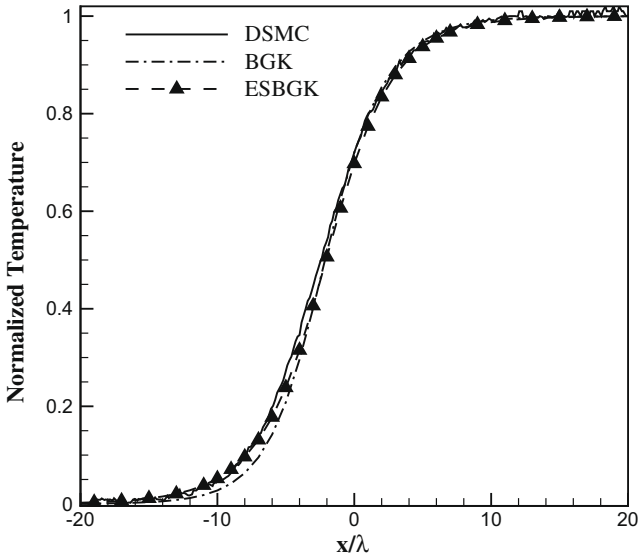

(b) Temperature profile.

Fig. 2. Normal shock structure, $M = 1.4$. Comparison of ES-BGK, BGK model with DSMC.

with ϵ being a small positive number to avoid the denominator becoming 0. SI_r is the smoothness indicator function defined by

$$SI_r = \int |\Delta x_i|^{2l-1} \left(\frac{\partial^l p^{(r)}(x)}{\partial^l x^2} \right) dx \tag{19}$$

It should be mentioned that there are other smoothness indicators that are minor variations of the smoothness indicator mentioned here. For each cell, the constants $c_i^{(r)}$, $d^{(r)}$ are precomputed. For a uniform mesh, it is sufficient to calculate them once, whereas for a non-uniform mesh, they are cell-dependent and have to be computed for each cell.

4.3. Runge–Kutta time marching scheme

In order to ensure high-order accuracy in time integration, we use second- and third-order Total Variation Diminishing (TVD) Runge–Kutta schemes described by Zhou et al. [14]. In the following discussion, f^n is the solution at time step n. The operator L refers to

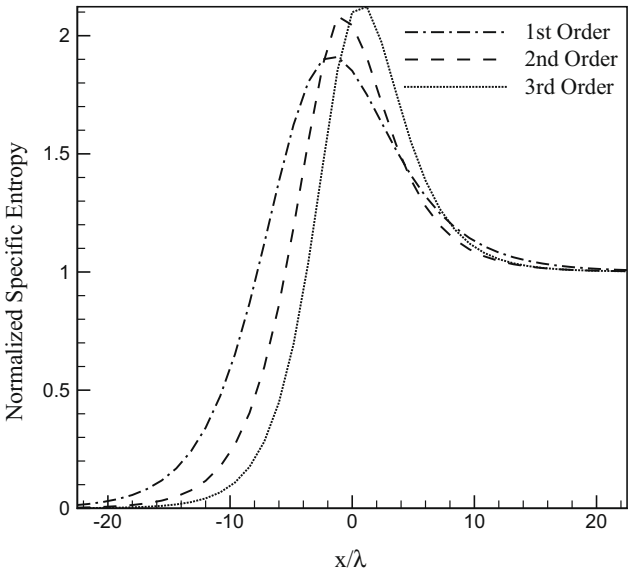

(a) 50 cells

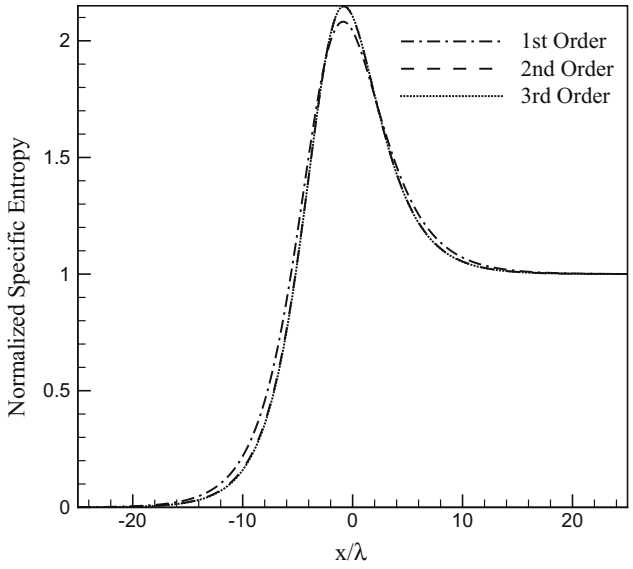

(b) 200 cells

Fig. 3. Normal shock structure. Specific entropy profile, $M = 1.4$.

$$L(f^n) = -\frac{1}{\Delta x}\left[F^n_{i+\frac{1}{2}j} - F^n_{i-\frac{1}{2}j}\right] - v_i\left(f^n - f^n_\gamma\right)$$

Second-order TVD:

$$\begin{aligned} f^{(1)} &= f^n + \Delta t L(f^n) \\ f^{n+1} &= \frac{1}{2}f^n + \frac{1}{2}f^{(1)} + \frac{1}{2}\Delta t L(f^{(1)}) \end{aligned} \tag{20}$$

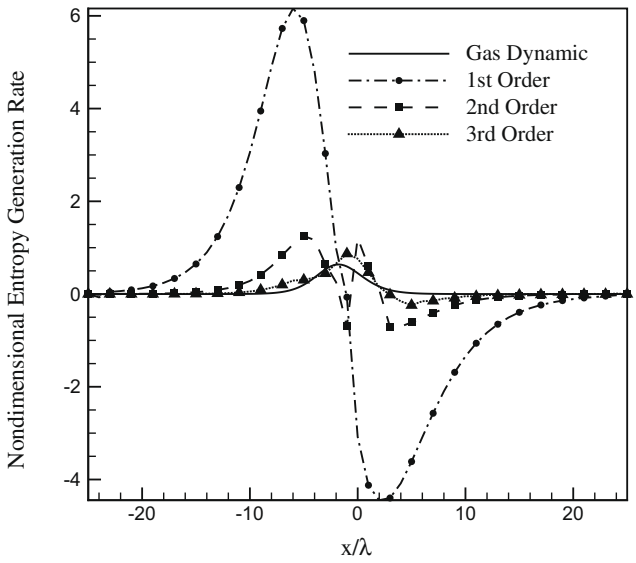

(a) 50 cells

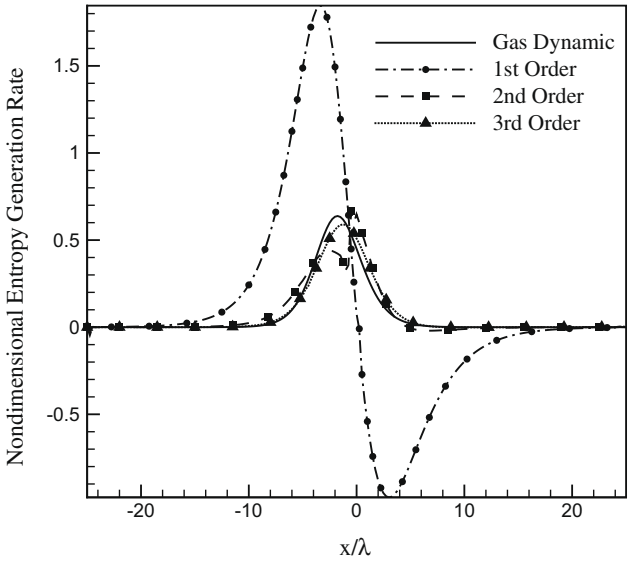

(b) 200 cells

Fig. 4. Normal shock structure. Entropy generation profile, $M = 1.4$.

Third-order TVD:

$$
\begin{aligned}
f^{(1)} &= f^n + \Delta t L(f^n) \\
f^{(2)} &= \frac{3}{4} f^n + \frac{1}{4} f^{(1)} + \frac{1}{4} \Delta t L(f^{(1)}) \\
f^{n+1} &= \frac{1}{3} f^n + \frac{2}{3} f^{(2)} + \frac{2}{3} \Delta t L(f^{(2)})
\end{aligned}
\tag{21}
$$

4.4. Calculation of entropy generation rate

The H-theorem states that the entropy generation rate, given by Eq. (4), is a strictly positive function. Due to numerical errors in space, time and velocity discretization, the discrete solution of Eq. (10), in general, may not satisfy the discrete version of the H-theorem. This is due to the fact that the discretized form of the moment transfer equation for entropy may not

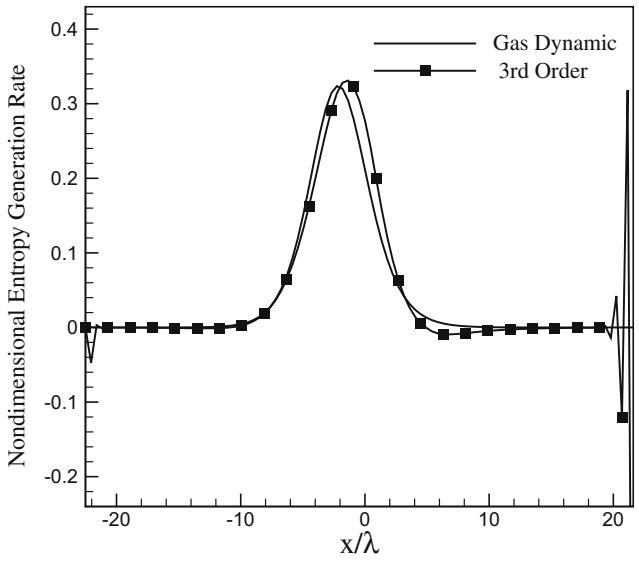

(a) Entropy generation profile

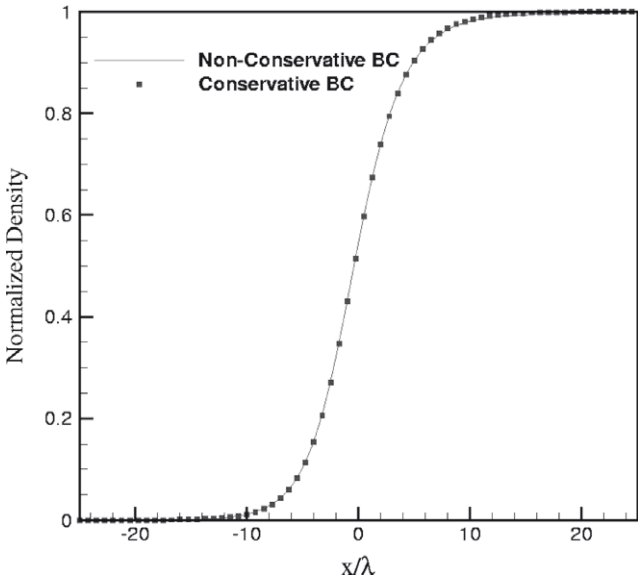

(b) Density profile

Fig. 5. Effect of non-conservative boundary conditions for shock wave at $M = 1.4$.

be satisfied for a distribution function which is obtained as a discrete solution of Eq. (10). The requirement that for a discrete solution of Eq. (10), the entropy generation rates calculated using discrete versions of Eqs. (3) and (8) are equal in magnitude, up to a certain precision, can be used as a criteria for accuracy of numerical simulations. The entropy generation rate obtained using the collision term can be calculated using the discretized form of Eq. (8) given by

$$\dot{S}_{coll_i} = -v \sum_j (f_{i,j} - f_{0_{i,j}}) \ln\left(\frac{h^3 f_{i,j}}{m^3}\right) \Delta c_j \tag{22}$$

The discrete velocity models for Eq. (9) have been formulated [12,16,17] such that the positivity of the entropy generation rate due to collisional relaxation, Eq. (22), is strictly enforced. However, numerical discretization as well as implementation errors may lead to significant deviation between the transport, Eq. (3), and collisional, Eq. (22), expressions for entropy generation rate.

Below, we present calculations of entropy generation rates for a normal shock wave, one-dimensional and two-dimensional shock tubes using various numerical schemes. The time and spatial derivatives in discretized form of Eq. (3) were

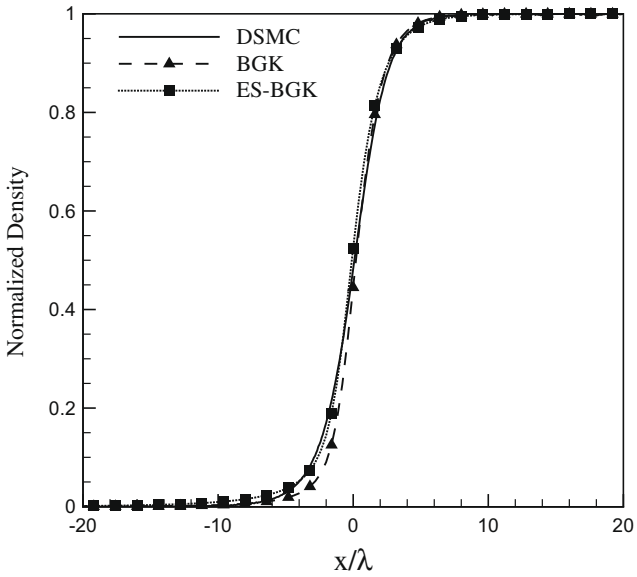

(a) Normalized density

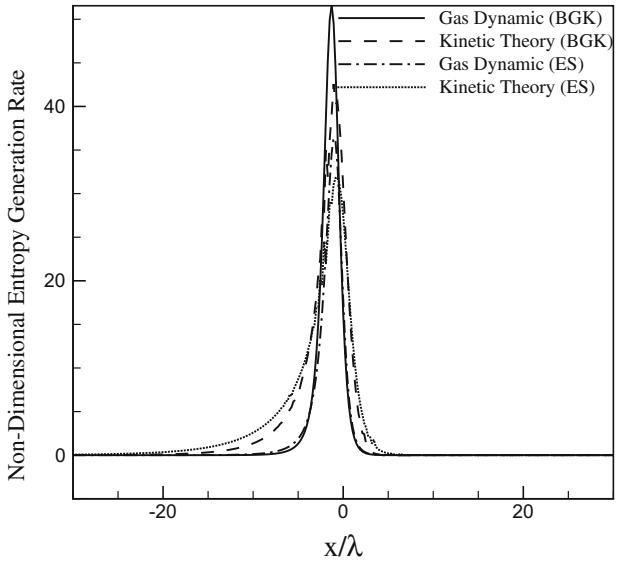

(b) Entropy generation rate

Fig. 6. Normal shock structure. Normalized density and entropy generation rate profiles, $M = 3.0$.

computed using a second-order central difference scheme and a third-order WENO scheme, respectively. The calculation of entropy generation rate is not computationally intensive and can be easily incorporated in the numerical procedure. As will be shown below the discretized version of H-theorem can be used as a convenient and powerful indicator of the accuracy of the numerical solution as well as of the onset of non-equilibrium.

5. Results and discussion

The model kinetic equations are applied to a steady problem and two unsteady problems. The steady problem considered is that of a stationary normal shock wave. Later, we solve and present solutions for two unsteady problems involving regions of non-equilibrium – a one-dimensional shock tube and a two-dimensional shock tube in which viscous effects are dominant due to the presence of walls. Second-order accurate fluxes are obtained using the minmod flux limiter and the third-order fluxes are computed using the WENO scheme. For the unsteady problems, second-order and third-order TVD Runge–Kutta

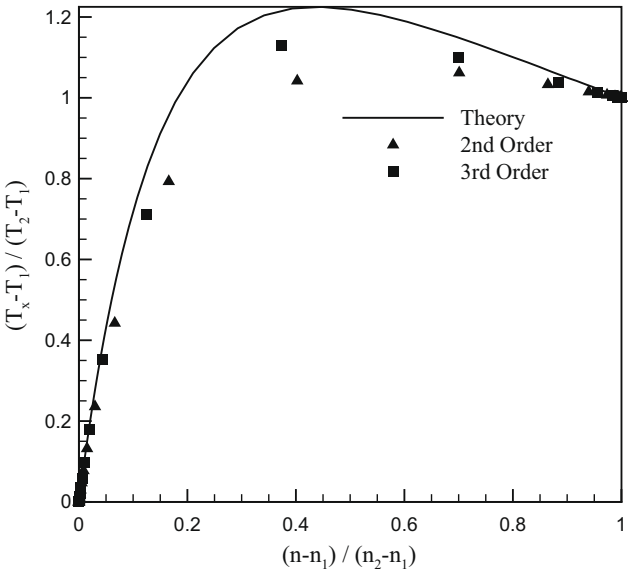

(a) 50 cells

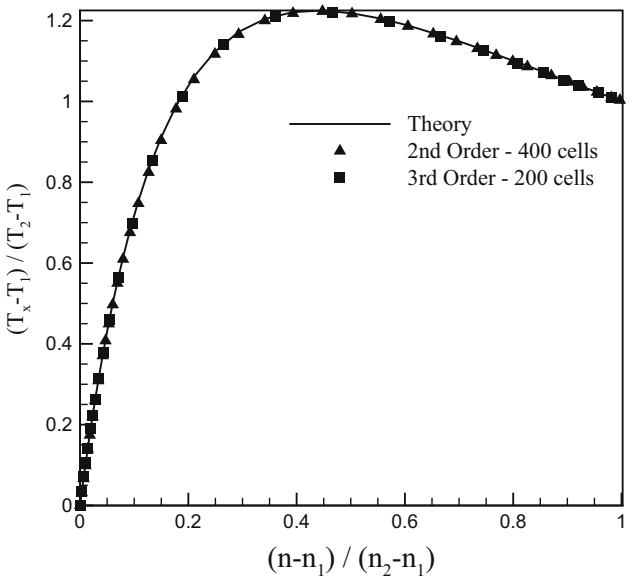

(b) Second-order scheme using 400 cells and third-order scheme using 200 cells

Fig. 7. Comparison of T_x profiles for a normal shock, $M = 3$.

schemes were used for time marching. All the numerical schemes were implemented in FORTRAN 90 and a parallel version was implemented for the two-dimensional problem using the MPI library.

5.1. Normal shock wave

First, we consider the structure of a stationary normal shock wave for different values of the upstream Mach number, $M_1 = 1.4$ and 3. The model kinetic equations were solved by using different flux schemes and the solutions obtained for the density and temperature profiles are compared with the solutions obtained using DSMC simulations. The macroparameters such as density, temperature and velocity in the computations were non-dimensionalized using the corresponding upstream values. In the figures below, the normalized temperature is $\frac{T-T_1}{T_2-T_1}$ where $T_1,\ T_2$ are upstream and downstream values,

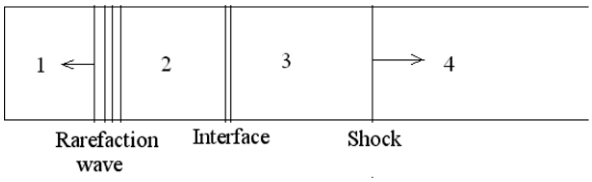

Fig. 8. Shock tube problem.

Table 2
1D shock tube: initial conditions to the left and right of interface.

Property	Left zone	Right zone
Density	1.0	0.1
x-Velocity	0	0
Temperature	1.0	1.0
Pressure	1.0	0.1

respectively. The reference speed is $c_\infty = \sqrt{2RT_\infty}$ and the reference time is L/c_∞ where L is the length of the domain ($50\lambda_1$ for a Mach number, $M = 1.4$) and λ_1 is the upstream mean free path. The specific entropy is non-dimensionalized by R, the universal gas constant. Entropy generation rate was non-dimensionalized by $\rho c_\infty R/L$. The steady state solution was assumed to have been reached when the L_2 norms of the change in non-dimensional density and temperature were both less than 10^{-6}.

The boundary conditions for the normal shock wave in argon gas with an upstream Mach number, $M = 1.4$ are shown in non-dimensionalized form in Table 1. The quantities upstream and downstream of the shock wave are related by the Rankine–Hugoniot relations.

The third-order WENO scheme requires significantly less CPU time and number of iterations for convergence, when compared to the other schemes. The DSMC solutions, shown in Figs. 1 and 2 for comparison with the kinetic solutions, were obtained using the Fortran code DSMC1S.FOR by Bird [18], with 300 cells and a total of about 19,400 molecules. The number density was 10^{20} and each simulated molecule represented 0.4×10^{16} real molecules. The average number of molecules per cell was 50 and 80 for cells upstream and downstream of the shock, respectively. A total of 8.74×10^4 iterations with a time step of 0.75×10^{-6} were needed to attain steady state. The macroparameters were sampled over another 58,000 time steps. The DSMC simulations took a total time of 1 h on a single processor. The deterministic kinetic solver took more than 24 h for convergence using the first-order scheme, 14 h with the second-order scheme and 8 h with the third-order scheme. Note that the same power-law viscosity model was used in the DSMC and the deterministic solver. The corresponding DSMC molecular model is the variable hard sphere (VHS) model with parameters given for argon in Ref. [18].

The results obtained using the ES collision model agree well with those obtained using DSMC. The comparison between density and temperature profiles obtained using different flux schemes and DSMC for the case of $M = 1.4$ is shown in Fig. 1(a) and (b). These were obtained using 50 cells in the physical space and 10 cells in each of the three directions in the velocity space. Fig. 2 compares the density and temperature profiles obtained using the BGK ($Pr = 1$), ES ($Pr = 2/3$) collision models using third-order WENO scheme, with the DSMC solution. The BGK model predicts a steeper shock profile because it over-predicts the collision frequency.

One of the key aspects discussed in this paper is the entropy generation rate and its effectiveness in characterizing the degree of non-equilibrium in the flow-field. Fig. 3 shows the specific entropy (entropy per unit mass) profile for the normal shock for the three different flux schemes. With 200 cells, the second- and third-order schemes give specific entropy profile with a maximum error of 0.04% but the second-order scheme does not predict the correct entropy generation rate profile. The gas dynamic entropy generation rate computed using the different flux schemes do not differ significantly from each other since the macroparameters obtained using different flux schemes differ only slightly. Hence in Fig. 4 we compare the entropy generation rates obtained using the gas dynamic definition equation (4) for third-order flux scheme and the kinetic theory definition equation (3) for the three different flux schemes. The entropy generation rate for all three flux schemes was computed using high-order derivatives and hence any difference is entirely due to the difference in the solutions for the distribution functions.

The entropy generation rate is shown to be a parameter that indicates the accuracy of the numerical solution. In the solution corresponding to 50 cells, shown in Fig. 4(a), all three flux schemes predict non-positive entropy generation rate which is clearly unphysical. However, while the third-order WENO scheme predicts a very small region of non-positive entropy generation rate, the second-order and first-order predict larger regions of non-positive entropy generation rate in the flow-field. The entropy generation rate predicted using the WENO third-order flux scheme with 200 cells in the physical space is positive in the entire flow-field and agrees well with the result predicted by the gas dynamic definition. Since, the upstream Mach number for this particular case is not very high, we expect the gas dynamic expression, that is valid for small deviations from equilibrium, to predict the regions of non-equilibrium accurately. The second-order solution using 200 cells does not indicate the presence of regions of non-positive entropy generation rate but does not agree well with that

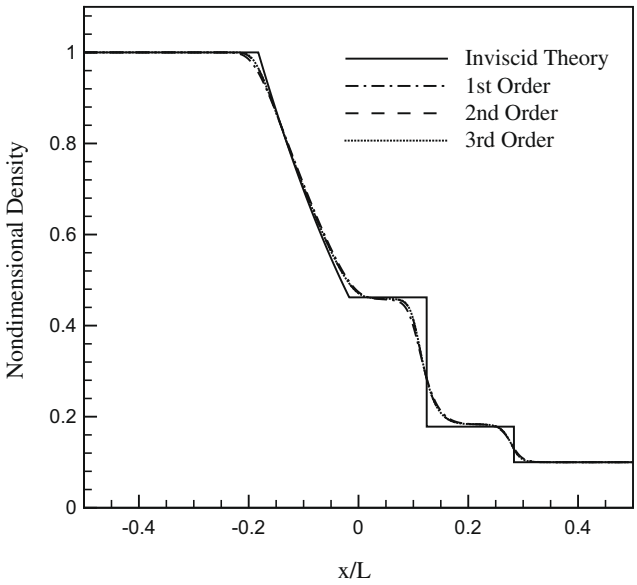

(a) Density

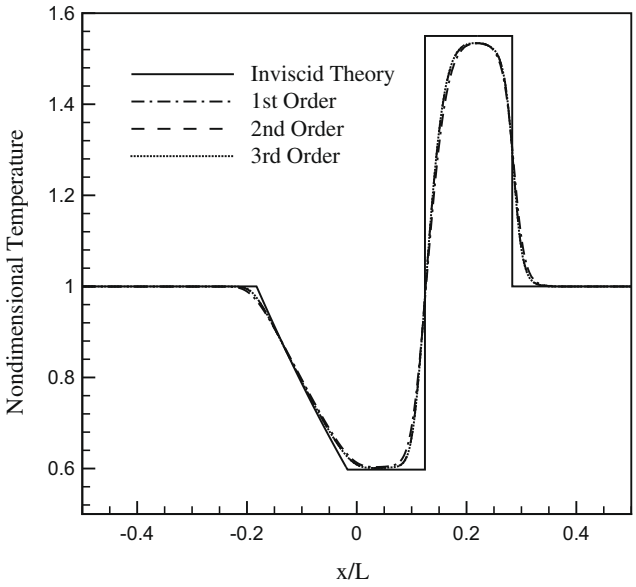

(b) Temperature

Fig. 9. Comparison of density and temperature profiles at non-dimensional time $t = 0.2$ for different flux schemes using 1000 cells.

obtained using the gas dynamic expression. The maximum magnitude of non-positive entropy generation for the first-order solution reduces from 120 for 50 cells (Fig. 4(a)) to 52 for 200 cells (Fig. 4(b)).

Entropy generation rate can also be an indicator of the correct implementation of the boundary conditions and size of the computational domain. For the simulation of a stationary normal shock wave, the boundary conditions upstream and downstream of the shock are related by the Rankine–Hugoniot equations. Now, the values of the macroscopic properties that are reconstructed from the discretized distribution functions do not satisfy the normal shock relations exactly and this shows up as oscillations in the entropy generation rate at the boundaries as shown in Fig. 5(a). However, it does not show up in the density, temperature or specific entropy profiles. Fig. 5(b) shows a comparison of the density profiles obtained using conservative and non-conservative boundary conditions. Depending on the error, the non-conservative boundary conditions can also lead to unrealistic phenomena such as the shifting phenomena which have been mentioned in earlier works [19,20]. The correct implementation of boundary conditions would be to solve the system of equations (mass, momentum and energy conservation) for the equilibrium distribution function that recovers the macroscopic properties exactly.

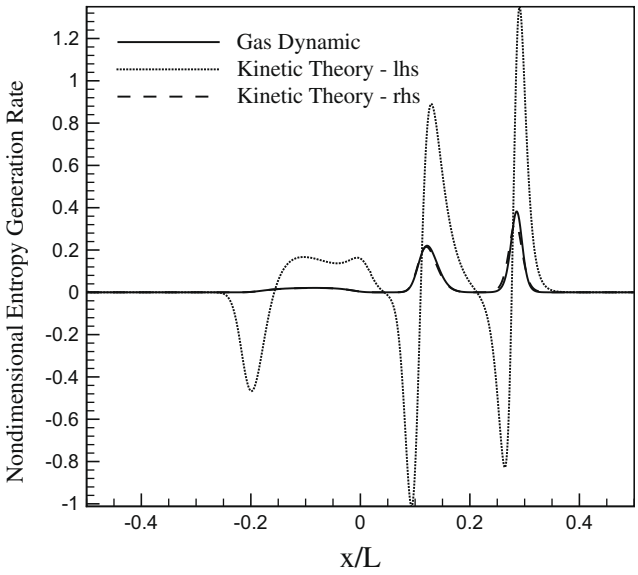

(a) First order flux scheme

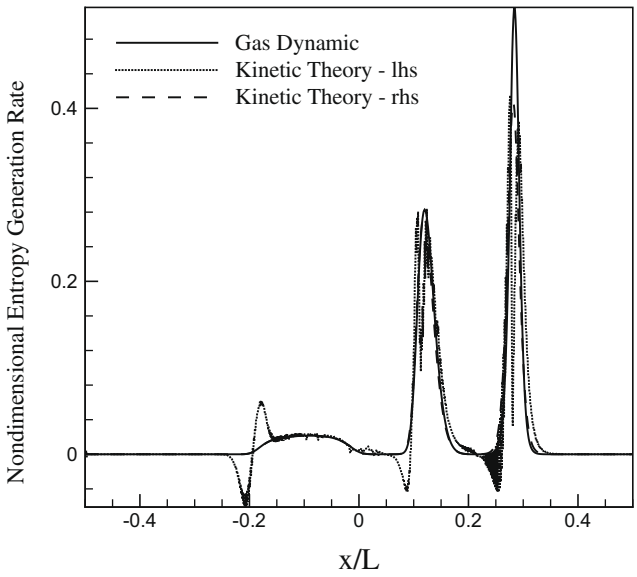

(b) Second order flux scheme

Fig. 10. Comparison of entropy generation rates at non-dimensional time $t = 0.2$ for first- and second-order flux schemes using 1000 cells.

We find that though the macroparameters are calculated based on a molecular approach, the gas dynamic expression for the entropy generation rate itself is insufficient to fully describe the non-equilibrium regions in the flow-field.

Now we consider a case of a strong non-equilibrium, the normal shock at Mach number 3.0. The solutions were again obtained using ES-BGK, BGK and DSMC computations. One of the important properties of a shock wave in a monatomic gas is the overshoot of temperature associated with the longitudinal component of thermal velocities [21]. From the conservation equations, it can be shown that, T_x is related to the number density n as follows

$$\frac{T_x}{T_1} = \frac{1}{3}\left[\left(5M_1^2 + 3\right)\frac{n_1}{n} - 5M_1^2\left(\frac{n_1}{n}\right)^2\right] \tag{23}$$

Differentiating the above expression, it can be shown that T_x possesses a maximum if M_1^2 is greater than 9/5. The analytical solution for T_x, can be used to compare the accuracy of the solutions obtained using different flux schemes. We present results for the variation of $(T_x - T_1)/(T_2 - T_1)$ as a function of $(n - n_1)/(n_2 - n_1)$ for $M_1 = 3$ to compare the results obtained

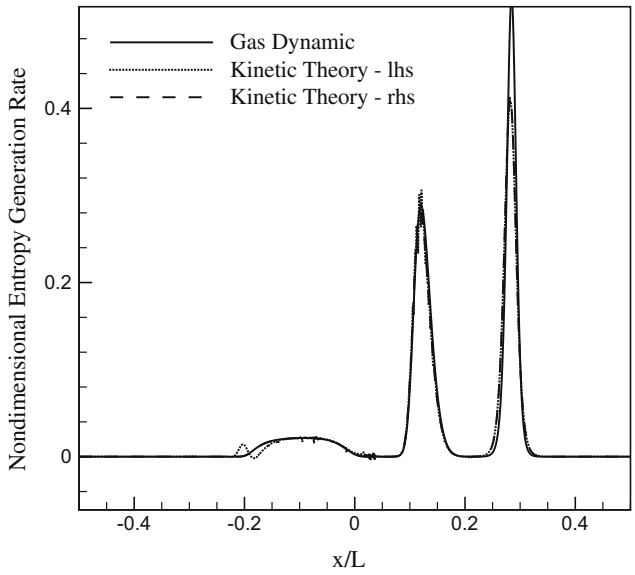

(a) Third order flux scheme

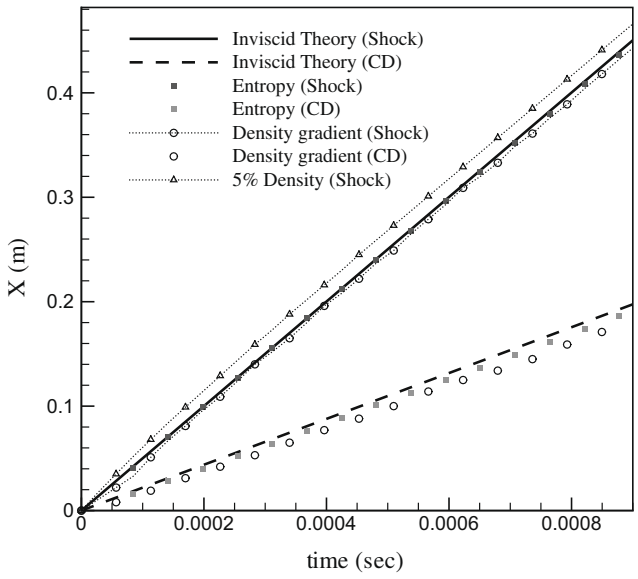

(b) Shock/CD locations

Fig. 11. (a) Entropy generation rate at non-dimensional time $t = 0.2$ for third-order WENO scheme using 1000 cells. (b) Shock/CD locations calculated from peaks in entropy generation rate.

using the second-order flux scheme and the third-order WENO scheme for a grid with 51 points. The solution is not fully converged in this case, but it provides a clear picture of the differences between the solution obtained using the two schemes. Fig. 7 shows a comparison of the variation of T_x and indicates that the result obtained by using 400 cells with the second-order flux scheme can be reproduced with a lesser number of cells using the third-order WENO scheme and both solutions match well with theory.

Fig. 6 shows the normalized density and entropy generation rate profiles for an upstream $M = 3.0$. The length of the computational domain was increased to 80λ in order to fully capture the region of non-equilibrium ahead of the shock wave. The number of cells was 400 in the physical space and the number of cells in the velocity space was increased to 14 in each direction. The results presented, compare the profiles obtained using both the BGK ($Pr = 1$) and the ES ($Pr = 2/3$) collision models. Clearly, the BGK model again predicts a steeper shock profile when compared to the ES model.

Table 3
Initial conditions for the different cases.

Property	Case 1	Case 2
ρ_0 (kg/m^3)	1.604E−4	1.604E−5
T_0 (K)	300	300
P_0 (Pa)	10	1

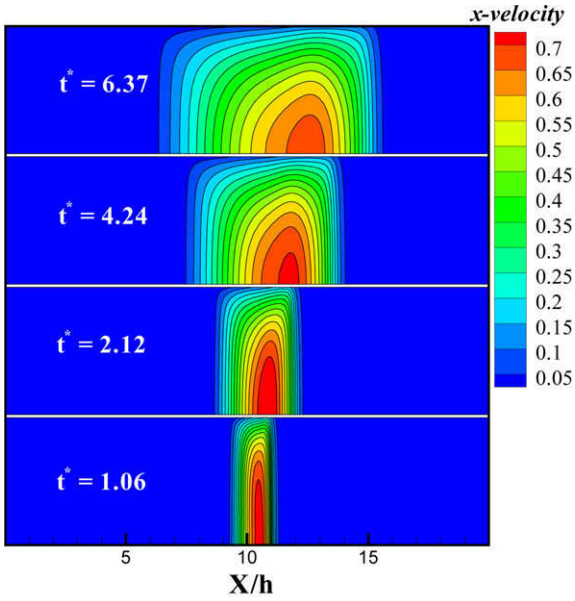

(a) Knudsen 0.01-0.1

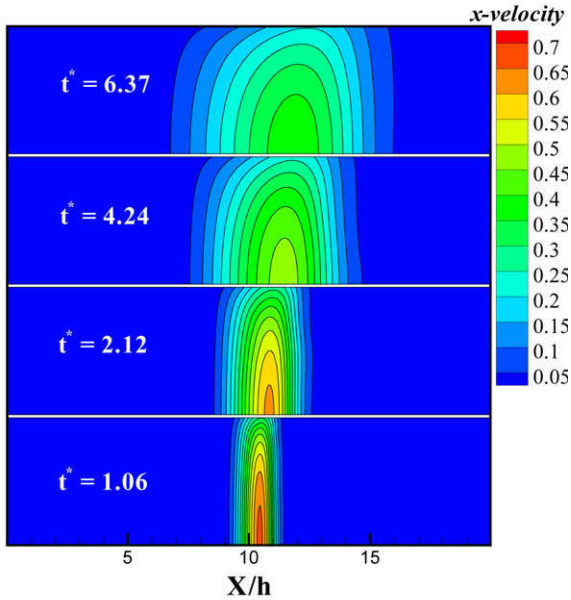

(b) Knudsen 0.1-1.0

Fig. 12. x-Velocity fields at four different instants of time.

Comparisons between the entropy generation rates obtained using the gas dynamic and the kinetic theory expressions show that, for a strong shock, the gas dynamic expression based only on the macroparameters fails to predict accurately, the region of non-equilibrium upstream of the shock. Schrock et al. [5] mention that the entropy generation rate based

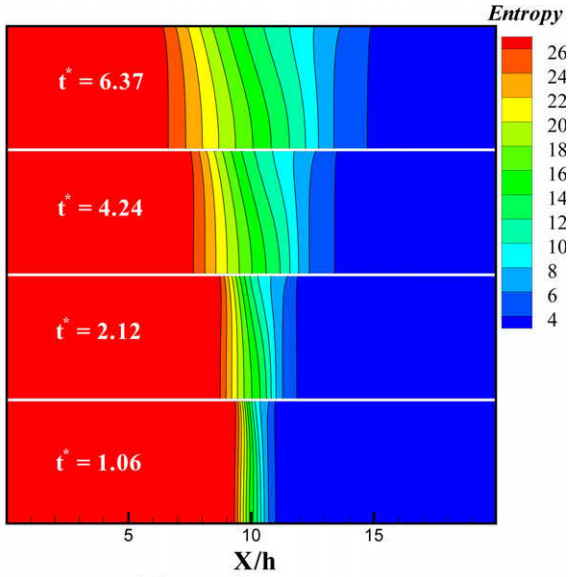

(a) Knudsen 0.01-0.1

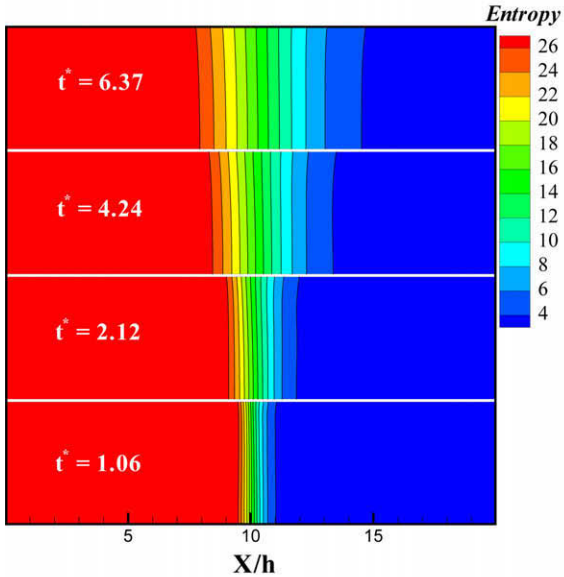

(b) Knudsen 0.1-1.0

Fig. 13. Entropy fields at four different instants of time.

on Navier–Stokes solutions do not completely capture the region of non-equilibrium in a shock wave. Note also the marked increase in the value of the entropy generation rate – from about 0.3 to 30 – as the Mach number is increased from 1.4 to 3.

5.2. 1D shock tube

A well-known one-dimensional unsteady flow problem is the Riemann problem [22], which treats the development of a flow due to an initial discontinuity. Removing the diaphragm separating the gas in the two reservoirs, results in a characteristic wave system consisting, in general, of three waves, a shock wave, an expansion fan, and a contact discontinuity. The inviscid shock tube problem can be solved exactly using gas dynamic theory. Fig. 8 shows a schematic of the Riemann problem.

The diaphragm in the shock tube is initially located at $x = L/2$ where L is the length of the domain. The argon gas to the left of the interface is at a pressure of 10 Pa and temperature 300 K. This corresponds to a density of 1.603×10^{-4} kg/m^3. The pressure on the right side of the interface is set to 1 Pa and temperature is set to 300 K. The initial conditions of various flow

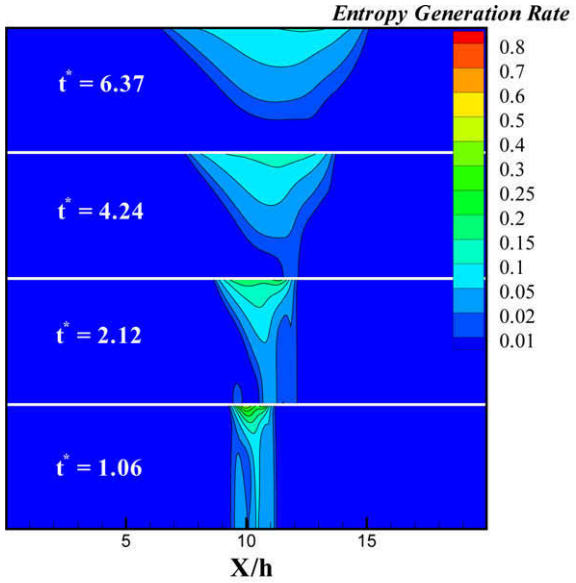

(a) Knudsen 0.01-0.1

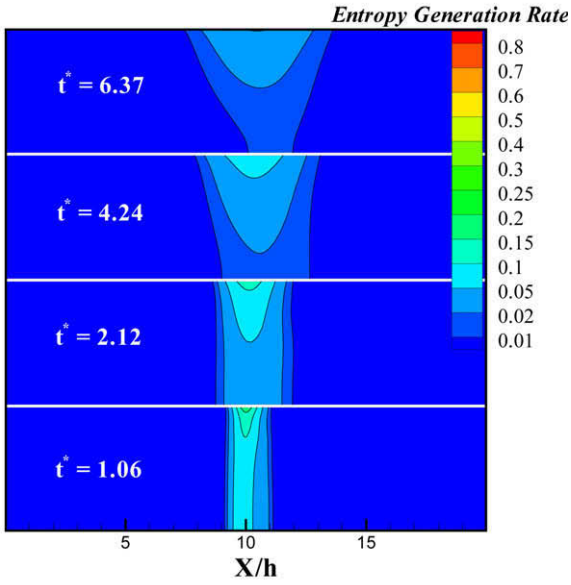

(b) Knudsen 0.1-1.0

Fig. 14. Entropy generation rate fields at four different instants of time for the two cases.

parameters are presented in non-dimensional form in Table 2. For the computations shown, the number of cells in the physical space for a grid converged solution is 1000. The velocity space was discretized using a $40 \times 20 \times 20$ grid. The entropy generation rate corresponding to the Riemann problem includes the unsteady component as opposed to the normal shock which is a steady state problem and is calculated using Eq. (3).

Entropy generation rate is shown to be a powerful indicator of grid convergence of the numerical solution in cases where observation of only the macroscopic parameters like density and temperature fail to capture the fact that the solution is not converged. Fig. 9 shows the density and temperature profiles obtained using various flux schemes and compares them with the solution obtained using inviscid theory. It can be seen that the profiles obtained using various flux schemes agree extremely well. The solutions obtained using first-order and second-order schemes differ by less than 1% and 0.1% from the third-order scheme, respectively. Fig. 10 shows the entropy generation rate profiles obtained using the first-order and second-order flux schemes and it can be clearly seen that the solution predicts regions of non-positive entropy generation rate. However, the entropy generation rate profile for solution obtained using the third-order WENO scheme, shown in Fig. 11, agrees well with the gas dynamic expression and also with the entropy generation rate obtained using the collision term.

The three peaks in the entropy generation rate profile in Fig. 11 a from right to left correspond to the location of shock, contact discontinuity and rarefaction fan, respectively. Their locations and velocities can then be calculated by tracking these peaks over time [23]. For comparison with experimental data, it is important to be able to predict the velocities of shockwave and other flow structures. One method to calculate the shock wave velocity from numerical solution is to track the location where the density is equal to a small fixed value above density of the unperturbed driven gas. For example, a value of 5% has been used in the 5% density method [24]. Another method that can be used is the steepest gradient method where the locations of shockwave and contact discontinuity are points with maximum gradient in density, i.e. $max\left(|\frac{d\rho}{dx}|\right)$.

Fig. 11 shows the locations of shock and contact discontinuity based on inviscid theory, ES-BGK solution, steepest gradient in density and 5% density methods. The maximum error in location of shock is less than 0.7% for the ES-BGK solution using the peaks in entropy generation rate. Thus, entropy generation rate can be a useful quantity in calculating the location and velocity of both the shock wave and contact discontinuity. This can be extended further to study the rarefaction effects and shock speed attenuation by boundary layer interaction in 2D shock tube [25] as discussed below.

5.3. 2D shock tube

The dimensions of shock tubes that are typically used in laboratories, ensure that the boundary layer effects due to the presence of walls are negligible and the problem can be considered to be one-dimensional for all practical purposes making it similar to the Riemann problem described in the previous subsection. However, to get high Mach numbers, the initial pressure ratio required across the diaphragm is extremely high thereby increasing the burden on vacuum pumps. In case a desktop shock tube were used, it is easier and faster to pump down the chambers to obtain the high pressure ratios due to their smaller dimensions. But as the size of the shock tube is reduced, the boundary layer effects are no longer negligible [26]. Shocks are also widely used to induce faster combustion and their use in microdevices is an active area of research [27,24]. Here, we consider the two-dimensional flow in a shock tube in which the viscous effects due to the presence of walls are dominant and the shock is curved due to energy dissipation in the boundary layer. We present results for the simulation of two cases, with Knudsen numbers (Kn) in the range 0.01–1, solved using the kinetic model equations.

The length and height of the shock tube were chosen to be 1 and 0.05 m, respectively. The pressures in the high and low pressure zones for Case 1 were fixed such that the corresponding Knudsen numbers were 0.01 and 0.1, respectively. The temperatures of the undisturbed driver and driven gases were set to 300 K. The temperature of the walls of the shock tube was fixed at 300 K. To reduce the computational cost, the symmetry of the problem was used to reduce the domain size with the use of a symmetry boundary condition at the plane of symmetry. The dimension of the phase space in the Kinetic WENO solver is fixed as $320 \times 24 \times 20 \times 20 \times 10$. The cells in the x-direction were uniformly spaced while a non-uniform cell size was chosen for the y-direction in order to capture details close to the walls. A successive ratio of 1.1 was used for the non-uniform cell size distribution in the y-direction. Case 2 was run with the same grid resolution and pressure ratio but at a lower pressure as shown in Table 3. The Knudsen number in the left zone is 0.1 and in the right zone is 1.0. Case 2 gives profiles very different from Case 1 that are the manifestation of rarefaction effects.

Figs. 12 and 13 show the maps of x-velocity and entropy at four different instants of time $t^* = 1.06, 2.12, 4.24, 6.37$ where $t^* = 1$ corresponds to the theoretical time it takes for the shock to move a distance equal to the width of the shock tube. As time progresses, the zone of non-equilibrium expands and its extent can be found from the entropy generation rate profiles. At the plane of symmetry, the contours of entropy generation rate show three peaks corresponding to three different regions of non-equilibrium – the compression wave, the contact discontinuity, and the rarefaction wave. At the walls of the shock tube, the interactions between the boundary layer and the wave system, lead to a more complicated interaction indicating only one distinct peak in the entropy generation rate contours. Also, Fig. 14 shows that the maximum entropy generation rate in an unsteady shock tube occurs in the boundary layer and shock wave interaction region.

6. Conclusions

We have proposed the use of a discrete version of H-theorem for analysis of numerical accuracy of rarefied flow simulations. Additionally, entropy generation rate has been investigated as an indicator of the onset of non-equilibrium which can be applied as a breakdown parameter in hybrid continuum/rarefied flow simulations. The numerical solution of Boltzmann model kinetic equations is obtained using the first-, second- and third-order flux schemes in the finite volume method. The solution is verified by comparison with the DSMC simulations for a normal shock problem. For a normal shock at a low Mach number, $M = 1.4$, the entropy generation rate based on the gas dynamics and kinetic theory agree well. However, at a higher Mach number, $M = 3$, the gas dynamic entropy generation rate is shown to deviate significantly from the that based on kinetic theory. The use of entropy to assess equilibrium breakdown in unsteady flows is elucidated on the examples of Riemann problem and two-dimensional shock tube. For 1D shock tube, the maximum values of entropy generation rate correspond to the instantaneous locations of shock wave and contact discontinuity, whereas the zone of rarefaction waves are characterized by a much lower values of entropy generation. The maximum entropy generation rate in a 2D shock tube occurs in the boundary layer and shock wave interaction region. The simulations indicate that a non-dimensional entropy generation rate of 0.1 corresponds to a significant deviation from equilibrium and strong non-equilibrium can be characterized by a value greater than 0.3. Entropy generation rate has shown to be a powerful indicator for both accuracy of the

numerical solution in terms of mesh convergence and compatibility of boundary conditions as well as for identification of continuum breakdown.

Acknowledgments

This work has been supported by Purdue Research Foundation and Department of Energy [National Nuclear Security Administration] under award No. DE-FC52-08NA28617.

References

[1] R. Roveda, D.B. Goldstein, P.L. Varghese, Hybrid Euler/particle approach for continuum/rarefied flows, Journal of Spacecraft and Rockets 35 (1998) 258–265.
[2] J.M. Burt, I.D. Boyd, A hybrid particle approach for continuum and rarefied flow simulation, Journal of Computational Physics 228 (2009) 460–475.
[3] V. Kolobov, R. Arslanbekov, V. Aristov, A. Frolova, S. Zabelok, Unified solver for rarefied and continuum flows with adaptive mesh and algorithm refinement, Journal of Computational Physics 223 (2007) 589–608.
[4] C.R. Schrock, R.J. McMullan, J.A. Camberos, Calculation of entropy generation rates via DSMC with application to continuum/equilibrium onset, in: Proceedings of the 38th AIAA Thermophysics Conference, AIAA Paper 2005-4830, Toronto, Ontario, Canada, 2005.
[5] C.R. Schrock, R.J. McMullan, J.A. Camberos, Continuum onset parameter based on entropy gradients using Boltzmann's *H*-theorem, in: Proceedings of the 43rd AIAA Aerospace Sciences Meeting and Exhibit, AIAA-2005-967, Reno, Nevada, 2005.
[6] G.F. Naterer, J.A. Camberos, Entropy and the second law fluid flow and heat transfer simulation, Journal of Thermophysics and Heat Transfer 17 (3) (2003) 360–371.
[7] L. Boltzmann, Lectures on Gas Theory, Dover Publication, 1995.
[8] P.L. Bhatnagar, E.P. Gross, M. Krook, A model for collision processes in gases. I. Small amplitude processes in charged and neutral one component systems, Physical Review 94 (1954) 511.
[9] M. Krook, Continuum equations in the dynamics of rarefied gases, Journal of Fluid Mechanics 6 (1959) 523.
[10] P. Andries, P.Le. Tallec, J. Perlat, B. Perthame, The Gaussian–BGK model of Boltzmann equation with small Prandtl numbers, European Journal of Mechanics B: Fluids 19 (2000) 83.
[11] L.H. Holway, New statistical models for kinetic theory: methods of construction, Physics of Fluids 9 (1966) 1658.
[12] L. Mieussens, H. Struchtrup, Numerical comparison of Bhatnagar–Gross–Krook models with proper Prandtl number, Physics of Fluids 16 (8) (2004) 2797–2813.
[13] A. Harten, S. Osher, Uniformly high-order accurate non-oscillatory schemes, SIAM Journal of Numerical Analysis 24 (1987) 279–309.
[14] T. Zhou, Y. Li, C.-W. Shu, Numerical comparison of WENO finite volume and Runge–Kutta discontinuous Galerkin methods, Journal of Scientific Computing 16 (2) (2001) 145–177.
[15] C.-W. Shu, Essentially Non-Oscillatory and Weighted Essentially Non-Oscillatory Schemes for Hyperbolic Conservation Laws, NASA/CR-97-206253, NASA Langley Research Center, Hampton, VA, November 1997.
[16] L. Mieussens, H. Struchtrup, Discrete-velocity models and numerical schemes for the Boltzmann–BGK equation in plane and axisymmetric geometries, Journal of Computational Physics 162 (2) (2000) 429–466.
[17] A. Frezzotti, Numerical investigation of the strong evaporation of a polyatomic gas, in: Proceedings of the 17th Symposium on Rarefied Gas Dynamics, 1991.
[18] G.A. Bird, Molecular Gas Dynamics and the Direct Simulation of Gas Flows, second ed., Oxford University Press, New York, 1994.
[19] T. Ohwada, Structure of normal shock waves: direct numerical analysis of the Boltzmann equation for hard-sphere molecules, Physics of Fluids 5 (1) (1993) 217–234.
[20] P. Degond, J.-G. Liu, L. Mieussens, Macroscopic fluid models with localized kinetic upscaling effects, Multiscale Modelling and Simulation 5 (3) (2006) 940–980.
[21] S.-M. Yen, Temperature overshoot in shock waves, Physics of Fluids 9 (7) (1966) 1417–1418.
[22] S. Schreier, Compressible Flow, second ed., Wiley, New York, 1982.
[23] S. Chigullapalli, A. Venkattraman, A.A. Alexeenko, M.S. Ivanov, Non-equilibrium flow modeling using high-order schemes for the Boltzmann model equations, in: Proceedings of the 40th Thermophysics Conference, AIAA Paper 2008-3929, Seattle, Washington, 2008.
[24] D.E. Zeitoun, Y. Burtschell, I.A. Graur, M.S. Ivanov, A.N. Kudryavtsev, Ye.A. Bondar, Numerical simulation of shock wave propagation in microchannels using continuum and kinetic approaches, Shock Waves 19 (4) (2009) 307–316.
[25] S. Chigullapalli, A. Venkattraman, A.A. Alexeenko, Modeling of viscous shock tube using ES-BGK model kinetic equations, in: Proceedings of the 47th AIAA Aerospace Sciences Meeting, AIAA Paper 2009-1317, Orlando, FL, 2009.
[26] F. Iancu, N. Muller, Efficiency of shock wave compression in a microchannel, Microfluidics and Nanofluidics 2 (2006) 50–63.
[27] M. Brouillette, Shock waves at microscales, Shock Waves 13 (2003) 3–12.